IMA Journal of Numerical Analysis (2008) Page 1 of 28
doi: 10.1093/imanum/dri000

Comparisons between pseudospectral and radial basis function derivative approximations

BENGT FORNBERG
Department of Applied Mathematics, University of Colorado
Boulder, CO 80309, USA (fornberg@colorado.edu)

NATASHA FLYER
Institute for Mathematics Applied to Geosciences, National Center for Atmospheric Research
Boulder, CO 80307, USA (flyer@ucar.edu)

JENNIFER M. RUSSELL
Same address as first author, (Jennifer.Russell@colorado.edu)

Fourier-based pseudospectral (PS) methods have been used since the 1970s for obtaining spectrally accurate solutions to PDEs in periodic geometries. Radial basis functions (RBFs) were introduced about the same time for interpolation on scattered nodes in irregular geometries. As was later recognized, they can also be used for accurate numerical solution of PDEs. Although the main strength of RBFs lies in their outstanding geometric flexibility, offering possibilities of spectral accuracy also over irregularly shaped finite domains, it is still of interest to compare them against Fourier-based PS methods in the extremely simple geometries (infinite or periodic domains) where the latter can also be used. Mostly by means of heuristic arguments and graphical illustrations based on Fourier analysis and numerical experiments, we show that there are notable differences (more pronounced in increasing numbers of dimensions) in how the two spectral approaches approximate derivatives.

Keywords:
Pseudospectral, PS, radial basis functions, RBF, derivative approximations, accuracy, Celtic cross

1. Introduction

One of Ron Mitchell's main areas of interest concerned relations between derivative approximations in 1-D compared to those in multi-dimensions (Mitchell & Fairweather (1964), Fairweather & Mitchell (1967), Gourlay & Mitchell (1969), Gourlay & Mitchell (1969)). In the present article, dedicated to his memory, we note that this issue again becomes very relevant in the context of understanding the accuracy of radial basis function (RBF) approximations, especially in comparison with pseudospectral (PS) approximations.

A key feature of RBF-based approximations for solving PDEs is that they allow spectral accuracy to be combined with very general types of local node refinement over irregularly shaped domains (Flyer & Lehto (2008)). Although formal proofs for spectral convergence are few and of limited scope, the key issue is not to allow any Runge phenomenon-like issues to develop (Fornberg & Zuev (2007)). In some recent test cases where both RBF and PS approaches have been applicable, RBF methods were found to offer significantly higher accuracy for the same number of nodes (Larsson & Fornberg (2003), Flyer & Wright (2007), Flyer & Wright (2008)). This present study aims at providing additional understanding of why this often is the case, by means of examining how RBF and Fourier-PS methods approximate

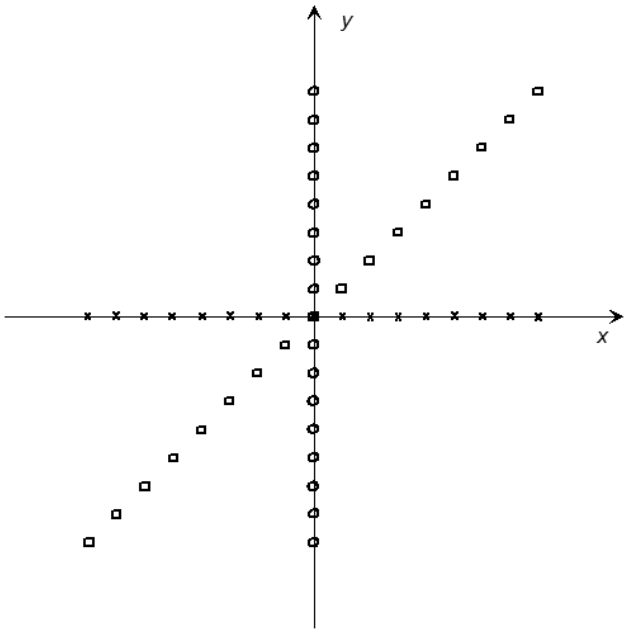

FIG. 1. PS stencils for approximating $\frac{\partial}{\partial x}$ (marked by " $\times$ ") and $\frac{\partial}{\partial y}$ (marked by "o"). The markers "□" indicate the direction corresponding to $\frac{1}{\sqrt{2}}(\frac{\partial}{\partial x}+\frac{\partial}{\partial y})$, along which no data is used in its PS approximation.

derivatives. We focus here on simple cases where there are no boundaries present (i.e. either infinite or periodic domains). In the presence of boundaries, RBF methods feature additional advantages in that boundary effects can be handled more effectively than by Chebyshev-type node clustering (which depletes nodes in the central regions of computational domains) (Fornberg et al. (2002)).

Although both RBF and PS methods can be applied in 1-D (and were for that situation compared in Fornberg & Flyer (2005)), what makes the two approaches genuinely different (even on regular grids) emerges most clearly only in higher dimensions. In order to gain insights into these matters, we focus the present work on 2-D, and start by noting that there is something quite strange about how a pseudospectral (PS) method on a 2-D Cartesian (rectangular) grid approximates the quantity $\frac{1}{\sqrt{2}}(\frac{\partial}{\partial x}+\frac{\partial}{\partial y})$. The quantity $\frac{\partial}{\partial x}$ at the center point in Figure 1 is approximated using the data values at the nodes marked by "x" and $\frac{\partial}{\partial y}$ using the ones marked "o". The quantity $\frac{1}{\sqrt{2}}(\frac{\partial}{\partial x}+\frac{\partial}{\partial y})$ is then obtained as a linear combination of these two results, i.e. the only data values used are those marked with either "x" or "o". However, this quantity $\frac{1}{\sqrt{2}}(\frac{\partial}{\partial x}+\frac{\partial}{\partial y})$ is the derivative in the direction marked by "□". In spite of this, not a single one of these points has been used. A derivative is a local property of a function, so it is counterintuitive to use nodes far out in two quite different directions (and with quite large weights - decaying only like $O(1/k)$ where k is the distance from the center) while ignoring available nearby information along the true direction of the derivative.

RBF approximations are global in nature, and usually combine the information from all the node points. In many cases they will pick up information that the PS approach ignores. We will obtain results along these lines via Fourier analysis on 2-D infinite lattices. While Cartesian lattice-type grids

are required for the PS approach, it will also transpire that this is not the optimal node layout for RBF approximations.

This study presents a variety of ideas, illustrations, and analysis relating to the concept of derivative approximations on infinite or periodic lattices. As mentioned above (and which cannot be stressed enough), this is not the situation for which RBFs typically are used. The main strength of infinitely smooth RBFs in actual computing resides in the fact that they can provide spectral accuracy even in cases of finite irregular geometries with local node refinements, etc., when PS methods are either severely degraded or entirely unavailable. In the 2-D periodic case, we also compare lattice-based node layouts against more irregular ones.

Sections 2 and 3 discuss PS methods on infinite Cartesian grids in 1-D and 2-D, respectively. RBFs are then introduced in Section 4, followed in Section 5 by a discussion of their properties on Cartesian and hexagonal infinite lattices. Since the issue of lattice-based versus scattered nodes is difficult to study on infinite domains, we address this instead on 2-D periodic domains in Section 6. Concluding remarks are given in Section 7.

Computational cost and numerical conditioning are important issues in practical RBF computations. Since they have been discussed extensively in the literature, we will only make some brief comments here. The computational cost per node usually is higher than for PS methods, although not always. For example, using Newton's method with Gaussian elimination to solve nonlinear PDEs leads to full matrices also in the PS case. Furthermore, there exist promising approaches for 'fast' RBF algorithms, summarized in Fasshauer (2007). The most straightforward RBF procedure (RBF-Direct; a direct implementation of equations (4.1) and (4.2)) becomes ill-conditioned in the case of relatively flat basis functions. This is inconvenient, but does not amount to a fundamental 'barrier'. The RBF-Direct procedure then consists of two successive unstable steps for computing a well conditioned result (Driscoll & Fornberg (2002), Fornberg et al. (2004), Schaback (2005)). The first numerical algorithms which demonstrated that genuinely stable numerics is completely feasible (in regular arithmetic precision, even in the flat basis function limit) were the Contour-Padé method Fornberg & Wright (2004) and the RBF-QR method by Fornberg & Piret (2007). Improvements and extensions of both of these methods are under development. Most likely, additional fully stable algorithms will be found in the future.

2. The PS method on an infinite grid in 1-D

On a 1-D unit-spaced ($h = 1$) infinite grid, only the Fourier modes $e^{i\,\xi\,x}$, $-\pi \leqslant \xi \leqslant \pi$ can be present. As a result of aliasing, any higher mode on the grid will be indistinguishable from a mode within this range. Using the Fourier transform (FT) convention $u(x) = \frac{1}{\sqrt{2\pi}} \int_{-\infty}^{\infty} \widehat{u}(\xi)\, e^{i\xi x} d\xi$, $\widehat{u}(\xi) = \frac{1}{\sqrt{2\pi}} \int_{-\infty}^{\infty} u(x)\, e^{-i\xi x} dx$), the relations between discrete node data $u(k)$ and how much there is present of each mode $\widehat{u}(\xi)$ become

$$u(k) = \frac{1}{\sqrt{2\pi}} \int_{-\pi}^{\pi} \widehat{u}(\xi)\, e^{-\,i\,\xi\,k} d\xi, \;\; k \in Z \tag{2.1}$$

where

$$\widehat{u}(\xi) = \frac{1}{\sqrt{2\pi}} \sum_{k=-\infty}^{\infty} u(k)\, e^{i\,\xi\,k} \quad , -\pi \leqslant \xi \leqslant \pi. \tag{2.2}$$

We can use (2.1) to evaluate $u(x)$ also for non-integer values of x, and thus obtain

$$u'(k) = \frac{1}{\sqrt{2\pi}} \int_{-\pi}^{\pi} (-i\xi)\, \widehat{u}(\xi)\, e^{-\,i\,\xi\,k} d\xi, \;\; k \in Z.$$

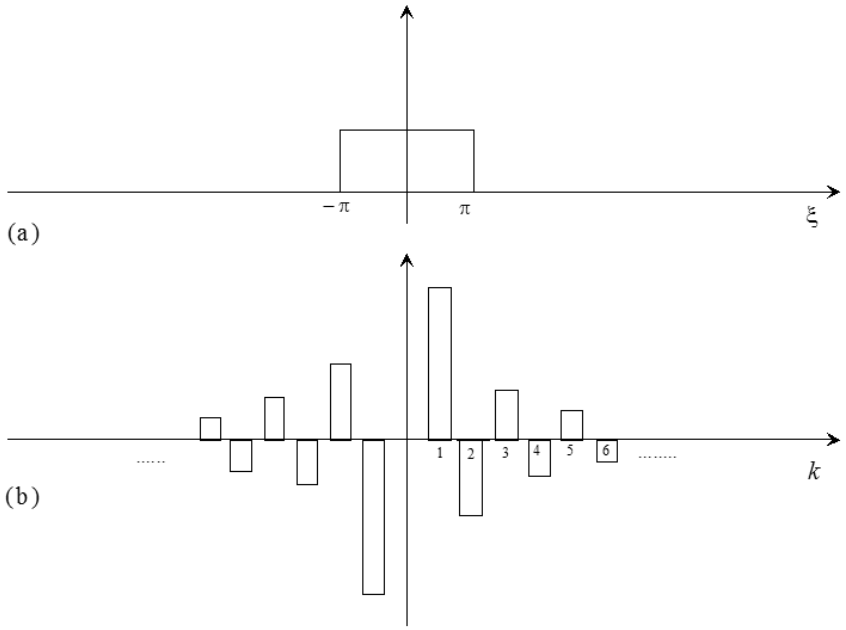

FIG. 2. (a) Fourier transform $\widehat{c}(\xi)$ in case of 1-D cardinal data, (b) FD coefficients w_k for PS approximation to $\frac{\partial}{\partial x}$.

In the case of cardinal data $c(k) = \begin{cases} 1 & k = 0 \\ 0 & \text{otherwise} \end{cases}, k \in Z$, we get $\widehat{c}(\xi) = \begin{cases} 1/\sqrt{2\pi} & -\pi \leqslant \xi \leqslant \pi \\ 0 & \text{otherwise} \end{cases}$,
as illustrated in Figure 2 a.

A Fourier-PS method is designed to be exact for all Fourier modes that the grid can represent. Converted over to global finite difference (FD) formulas (Fornberg (1996)), the FD weights w_k for $\frac{\partial}{\partial x}$, satisfying

$$u'(0) = \sum_{k=-\infty}^{\infty} w_k \, f(k)$$

therefore become

$$w_k = \frac{1}{2\pi} \int_{-\pi}^{\pi} (-i\xi) \, e^{-i\,\xi\,k} d\xi = \frac{\partial}{\partial x} \, \frac{\sin \pi x}{\pi x} \bigg|_{x=k} = \frac{(-1)^k}{k}, \tag{2.3}$$

as shown in Figure 2 b.

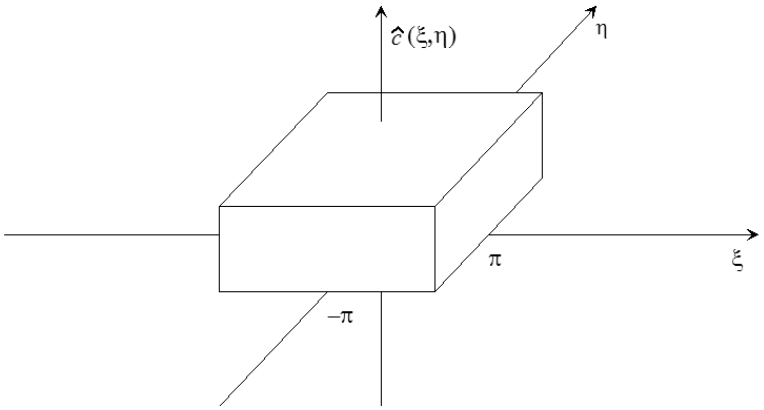

FIG. 3. Function $\widehat{c}(\xi,\eta)$ in the 2-D PS case.

3. PS and band limited derivative approximations in 2-D

3.1 *The PS method on an infinite Cartesian lattice*

The key formulas are in this case virtually identical to those in 1-D. The FT of cardinal data $c(k_1,k_2)$ becomes $\widehat{c}(\xi,\eta) = \begin{cases} 1/2\pi & -\pi \leqslant \xi,\eta \leqslant \pi \\ 0 & \text{otherwise} \end{cases}$ (Figure 3) and therefore

$$\left.\frac{\partial c(x,y)}{\partial x}\right|_{x=k_1,y=k_2} = \frac{1}{2\pi}\int_{-\pi}^{\pi}\int_{-\pi}^{\pi}(-i\xi)\, e^{-i(\xi k_1+\eta k_2)}d\xi d\eta$$
$$= \left(\frac{1}{\sqrt{2\pi}}\int_{-\pi}^{\pi}(-i\xi)\, e^{-i\,\xi\,k_1}d\xi\right)\left(\frac{1}{\sqrt{2\pi}}\int_{-\pi}^{\pi}e^{-i\,\eta\,k_2}d\eta\right).$$

The first factor recovers the 1-D result, and the second factor is one for $k_2 = 0$ and zero for other integer values of k_2. The FD weights for $\frac{\partial}{\partial x}$ will consequently extend only along the x-axis (Figure 4). From a numerical point of view, there is therefore no purpose in attempting to create fully 2-D PS stencils for quantities such as $\frac{\partial}{\partial x}$, $\frac{\partial}{\partial y}$, since this will not produce anything different from an immediate use of the standard 1-D formulas.

3.2 *Derivative approximations of band limited functions without any associated grid*

As we just observed, the 2-D lattice PS FD stencil for $\frac{\partial}{\partial x}$ simplified down to using the 1-D version in each spatial direction. Suppose instead that we are not confined to a rectangular lattice, and that we do not have any enforced special directions. The most natural variation to the Fourier transform shown in Figure 3 would be to consider a circular rather than a square area $[-\pi,\pi]\times[-\pi,\pi]$ within which $\widehat{c}(\xi,\eta)$ is constant and non-zero. If for example we choose a circular area of radius one, we obtain (most easily after an evaluation in polar coordinates)

$$c(x,y) = \frac{J_1(\sqrt{x^2+y^2})}{\sqrt{x^2+y^2}}\,, \tag{3.1}$$

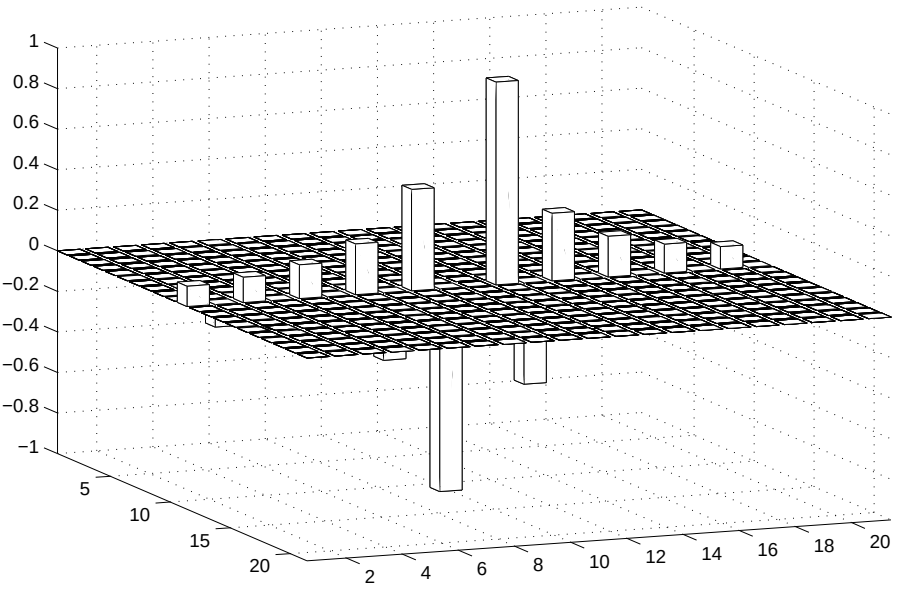

FIG. 4. FD weights in 2-D corresponding to $\frac{\partial}{\partial x}$ - exactly the same along the x-axis as in the 1-D case displayed in Figure 2 b.

from which follows

$$\frac{\partial}{\partial x}c(x,y) = \frac{x}{8}\ {}_0F_1(3,-\frac{1}{4}(x^2+y^2)) \tag{3.2}$$

(shown in Figure 5), and similarly

$$\frac{\partial}{\partial y}c(x,y) = \frac{y}{8}\ {}_0F_1(3,-\frac{1}{4}(x^2+y^2)), \tag{3.3}$$

where ${}_0F_1$ is a reduced form of the confluent hypergeometric function. These relations show that, once the Cartesian lattice concept has been removed, approximations for $\frac{\partial}{\partial x}$ and $\frac{\partial}{\partial y}$ will no longer be confined just to the x- and y-directions respectively, but will extend throughout a full vicinity of the center point. From (3.2) and (3.3) follow that the approximation for $\frac{1}{\sqrt{2}}(\frac{\partial}{\partial x}+\frac{\partial}{\partial y})$ will be exactly the same as for $\frac{\partial}{\partial x}$, but just turned 45^o (and similarly for any other angle as well). We have here again used the notation $c(x,y)$ because of the Fourier space similarity with grid-based cardinal functions (of which we will come across more examples later), in spite of the fact that the function defined in (3.1) is not associated with (or takes cardinal values on) any lattice-like node layout.

We will next introduce RBFs, and see how these approximate space derivatives.

4. Brief introduction to RBFs

With a *radial function* $\phi(r)$ and with data values f_k given at locations $\underline{x}_k$, $k = 1,2,\ldots,n$, the function

$$s(\underline{x}) = \sum_{k=1}^{n} \lambda_k\ \phi(||\underline{x}-\underline{x}_k||), \tag{4.1}$$

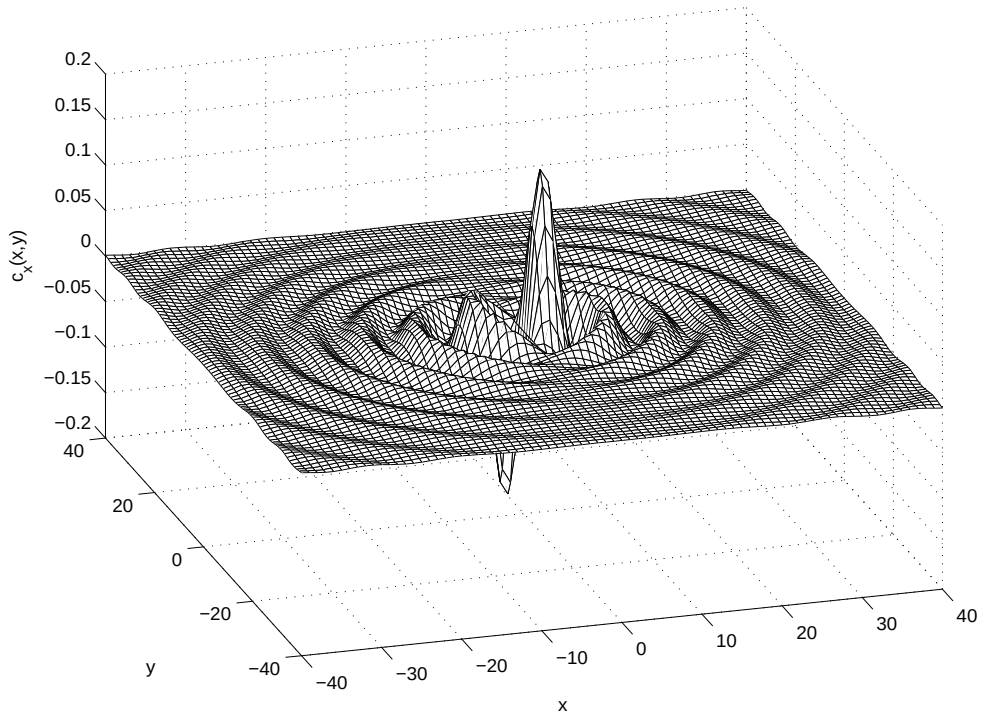

FIG. 5. The function by which data is to be weighted (convolved) in order to approximate $\frac{\partial}{\partial x}$ in the case of functions that are band limited in the sense that only Fourier modes obeying $\xi^2+\eta^2 \leqslant 1$ are included (For other bounds $\xi^2+\eta^2 \leqslant \rho^2$, the figure would differ only in terms of the scales along the axes).

Type of radial function			2-D **Fourier transform** $\widehat{\phi}(\rho)$
Piecewise smooth			
MN	monomial	$\lvert r\rvert^{2m+1}$	$(-1)^{m+1}\dfrac{((2m+1)!!)^2}{\lvert\rho\rvert^{2m+3}}$
TPS	thin plate spline	$\lvert r\rvert^{2m}\ln\lvert r\rvert$	$(-1)^{m+1}\dfrac{2^{2m}(m!)^2}{\lvert\rho\rvert^{2m+2}}$
Infinitely smooth			
MQ	multiquadric	$\sqrt{1+(\varepsilon r)^2}$	$-\dfrac{e^{-\frac{\lvert\rho\rvert}{\varepsilon}}(\varepsilon+\lvert\rho\rvert)}{\lvert\rho\rvert^3}$
IMQ	inverse MQ	$\dfrac{1}{\sqrt{1+(\varepsilon r)^2}}$	$\dfrac{e^{-\frac{\lvert\rho\rvert}{\varepsilon}}}{\varepsilon\,\lvert\rho\rvert}$
IQ	inverse quadratic	$\dfrac{1}{1+(\varepsilon r)^2}$	$\dfrac{K_0(\frac{\lvert\rho\rvert}{\varepsilon})}{\varepsilon^2}$
GA	Gaussian	$e^{-(\varepsilon r)^2}$	$\dfrac{e^{-\rho^2/(4\varepsilon^2)}}{2\varepsilon^2}$

Table 1. Definition and 2-D Fourier transforms for some cases of radial functions. For a similar table with Fourier transforms in n-D, see Fornberg et al. (2008).

where $\|\cdot\|$ denotes the standard Euclidean norm, interpolates the data if we choose the expansion coefficients λ_k in such way that $s(\underline{x}_k) = f_k$, $k = 1,2,\ldots,n$. The expansion coefficients λ_i can therefore be obtained by solving the linear system $A\,\underline{\lambda} = \underline{f}$ where

$$A_{i,j} = \phi(||\underline{x}_i - \underline{x}_j||). \tag{4.2}$$

The following are some key theorems regarding RBF interpolation. For proofs and further discussions, see for example Buhmann (2003), Wendland (2005), Fasshauer (2007):

- All the smooth RBF choices listed in Table 1 will give coefficient matrices A in (4.2) which are nonsingular, i.e. there is a unique interpolant of the form (4.1) no matter how the distinct data points are scattered in any number of space dimensions. In the cases of IQ, IMQ and GA, the matrix A is positive definite and, for MQ, it has one positive eigenvalue and the remaining ones all negative.

- Interpolation using MN and TPS can become singular in multi-dimensions. However, low degree polynomials can be added to the RBF interpolant to guarantee that the interpolation matrix is positive definite (a stronger condition than non-singularity). For example, for cubic RBF and TPS in d dimensions, this becomes the case if we use as interpolant $s(\underline{x}) = \sum_{k=1}^{d+1}\gamma_k p_k(\underline{x}) + \sum_{k=1}^{n}\lambda_k\,\phi(\|\underline{x}-\underline{x}_k\|)$ together with the constraints $\sum_{j=1}^{n}\lambda_j p_k(\underline{x}_j) = 0, k = 1,\ldots,d+1$. Here, $p_k(\underline{x})$ denotes a basis for polynomials of degree one in d dimensions, i.e. in the case of $d = 3$ (with $\underline{x} = (x_1,x_2,x_3)$), we have $p_1 = 1,\ p_2 = x_1,\ p_3 = x_2,\ p_4 = x_3$.

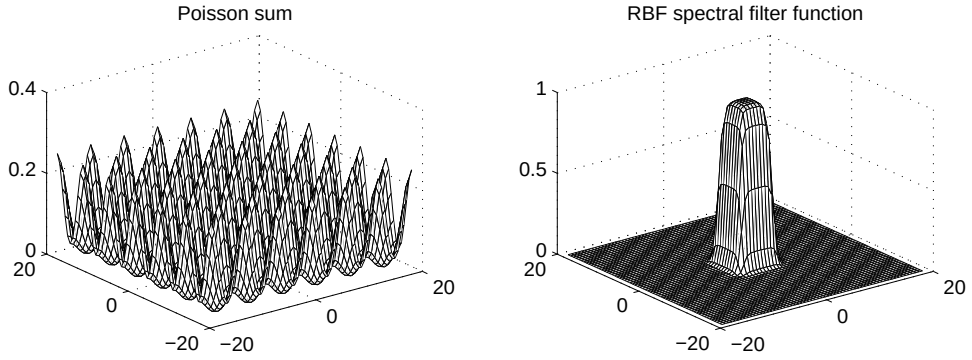

FIG. 6. (a) Poisson sum $\Xi_{Cart}(\xi,\eta)$ for GA, $\varepsilon = 1$ (b) Ratio $\widehat{\phi}(\xi,\eta)/\Xi_{Cart}(\xi,\eta)$.

- In 1-D, the RBF interpolant in the limit of $\varepsilon \to 0$ converges to the Lagrange interpolation polynomial (no matter how the distinct nodes are scattered) (Driscoll & Fornberg (2002)).
- For 1-D periodic data, this same limit reproduces standard trigonometric interpolants (again, for all node distributions). For scattered nodes on a sphere, it will in general reproduce the spherical harmonics (SPH) interpolant (Fornberg & Piret (2007)).

5. RBF interpolants and derivative approximations on infinite lattices

5.1 *Cartesian lattices*

As demonstrated in Buhmann & Powell (1990) the cardinal RBF interpolant on an infinite unit-spaced lattice (obeying $c(x,y) = \begin{cases} 1 & x,y = 0 \\ 0 & x,y \text{ other integers} \end{cases}$) can be written down explicitly:

$$c(x,y) = \frac{1}{4\pi^2} \int_{-\infty}^{\infty} \int_{-\infty}^{\infty} \frac{\widehat{\phi}(\xi,\eta) \cos x\xi \, \cos y\eta}{\Xi_{Cart}(\xi,\eta)} d\xi d\eta \tag{5.1}$$

where $\Xi_{Cart}(\xi,\eta)$ is the 2-D Poisson sum

$$\Xi_{Cart}(\xi,\eta) = \sum_{k=-\infty}^{\infty} \sum_{l=-\infty}^{\infty} \phi(k,l)\, e^{i(k\,\xi\, +\, l\,\eta)} = 2\pi \sum_{k=-\infty}^{\infty} \sum_{l=-\infty}^{\infty} \widehat{\phi}(\xi + 2\pi k, \eta + 2\pi l). \tag{5.2}$$

In many cases, the last form of the double sum in (5.2) is the most convenient one to use (and it also converges in many cases when the first double sum diverges). Table 1 lists the Fourier transforms $\widehat{\phi}(\xi,\eta)$ in the form $\widehat{\phi}(\rho)$ since they are rotationally symmetric, and therefore depend on $\rho = \sqrt{\xi^2 + \eta^2}$ only. For example, in the case of GA RBF with $\varepsilon = 1$, we obtain $\Xi_{Cart}(\xi,\eta)$ and $\widehat{\phi}(\xi,\eta)/\Xi_{Cart}(\xi,\eta)$, as shown in Figure 6.

Since $\Xi_{Cart}(\xi,\eta)$ is a doubly periodic sum of translates of $\widehat{\phi}(\xi,\eta)$, the ratio $\widehat{\phi}(\xi,\eta)/\Xi_{Cart}(\xi,\eta)$ will for $\varepsilon \to 0$ (when the spikes just get sharper) approach the same result $\widehat{\phi}(\xi,\eta) = \begin{cases} 1 & \xi,\eta \in [-\pi,\pi] \\ 0 & \text{otherwise} \end{cases}$

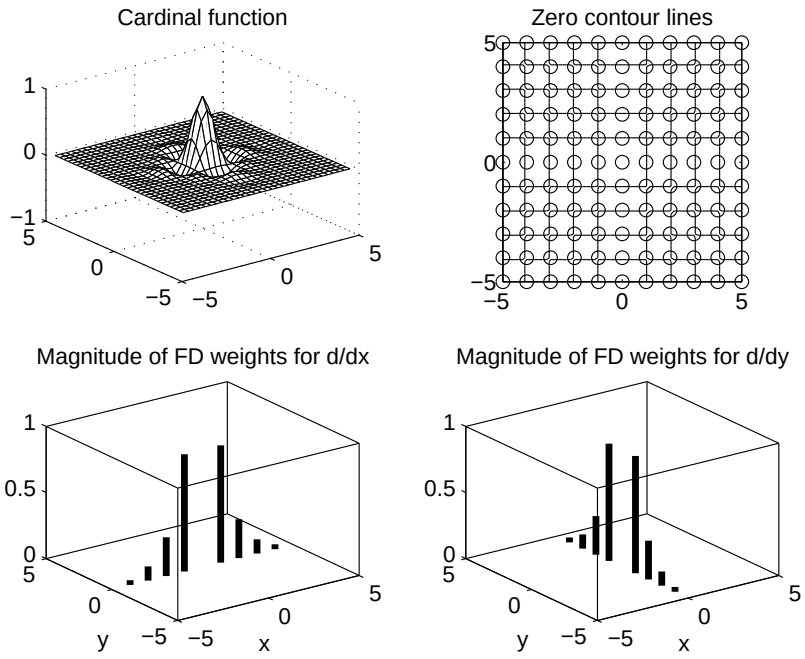

FIG. 7. Key properties of the GA cardinal RBF interpolant and the generated FD approximations in the case of Cartesian lattice and $\varepsilon = 1$.

as was illustrated for the PS case in Figure 3. The same result is true for any of the infinitely smooth RBF types in their $\varepsilon \to 0$ limit.

The equations (5.1) and (5.2) have in the past been utilized for numerous other investigations, such as analyzing *polynomial reproduction* (Powell (1992), Buhmann (2003), Flyer (2006)).

5.1.1 *Cardinal functions and resulting FD weights for* $\varepsilon > 0$ Based on (5.1), (5.2) and the Fourier transforms from Table 1, we can numerically calculate $c(x,y)$, $\frac{\partial}{\partial x}c(x,y)$, and $\frac{\partial}{\partial y}c(x,y)$, and then read off the corresponding FD weights as $-\frac{\partial}{\partial x}c(x,y)$ and $-\frac{\partial}{\partial y}c(x,y)$ at the lattice points. This provides the data that is displayed in Figures 7 and 8. The very simple set of zero contour lines that arises in the GA case (top right subplot of Figure 7; leading to FD stencils that extend only along the x- and y-axes respectively) is not typical for other types of smooth RBFs, as seen in the MQ case, illustrated in the Figure 8. Figure 9 shows a more detailed picture of the zero contour lines in the case of MQ with $\varepsilon = 1$ (revealing a striking resemblance to a Celtic cross). Similar changes in general 'pattern' in cardinal expansion coefficients and in interpolants at certain distances from the origin (increasing with ε decreasing) have been observed and analyzed earlier in other RBF contexts, e.g. (Fornberg & Flyer (2008), Fornberg et al. (2008)).

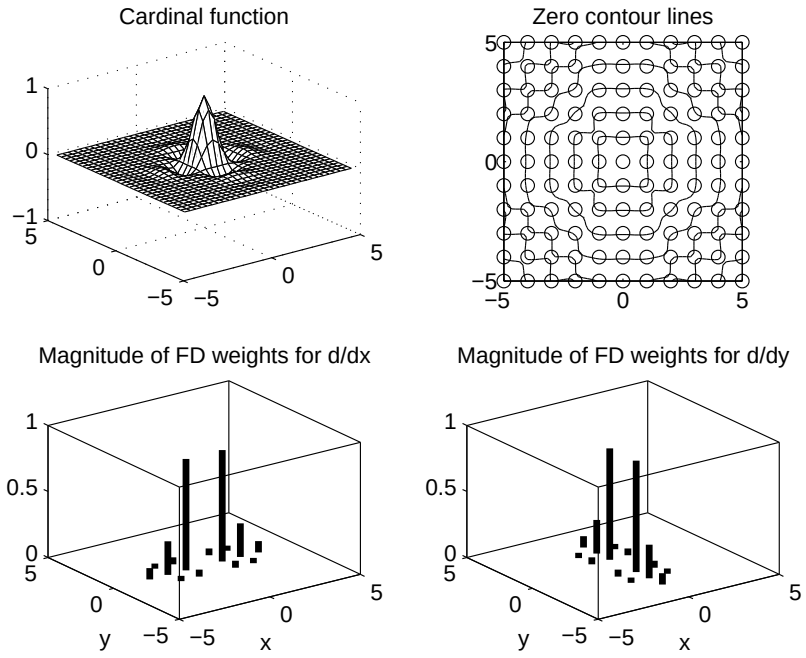

FIG. 8. Key properties of the MQ cardinal RBF interpolant and generated FD approximations in the case of Cartesian lattice and $\varepsilon = 1$. The weights are displayed only when exceeding 0.03 in magnitude.

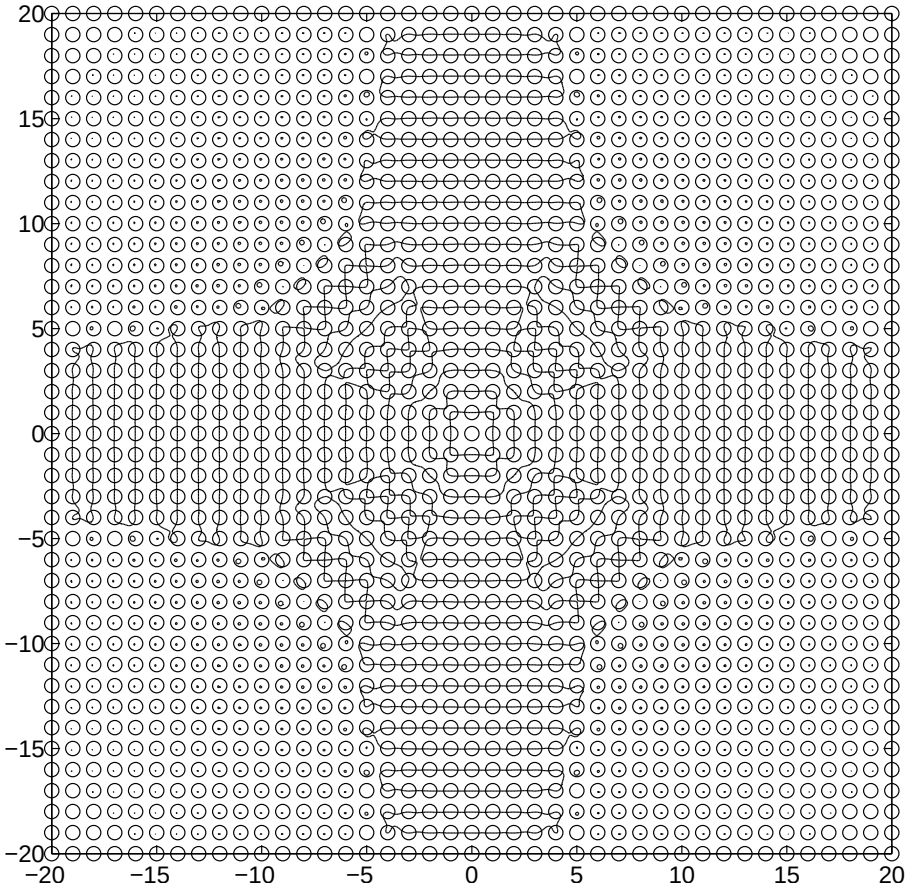

FIG. 9. Zero contour lines of the cardinal interpolant in the case of MQ RBFs with $\varepsilon = 1$.

5.1.2 *RBFs in the limit of* $\varepsilon \to 0$ In the limit of $\varepsilon \to 0$, we noted from the analysis at the start of Section 5.1 that the function $\widehat{\phi}(\xi,\eta)/\Xi(\xi,\eta)$ will approach $\widehat{c}(\xi,\eta)$, as shown in Figure 3, and will thus reproduce the 1-D PS differentiation formula. Consequently, the cardinal interpolant for *all* the smooth RBF types (just as in the PS case) will approach

$$c(x,y) = \frac{\sin \pi x}{\pi x} \, \frac{\sin \pi y}{\pi y}, \tag{5.3}$$

as was observed earlier by Baxter (1992). Based on this limit, we can immediately compute the results shown in Figure 10. The FD stencils will agree exactly with the PS case, as shown for $\frac{\partial}{\partial x}$ in Figure 4. According to (2.3), the weights decay to zero like $O(1/k)$. This should be compared to the finite ε results earlier in Figures 7 and 8, in which cases the decay is exponential (obtained from the Fourier transforms of infinitely differentiable functions rather than from a discontinuous one).

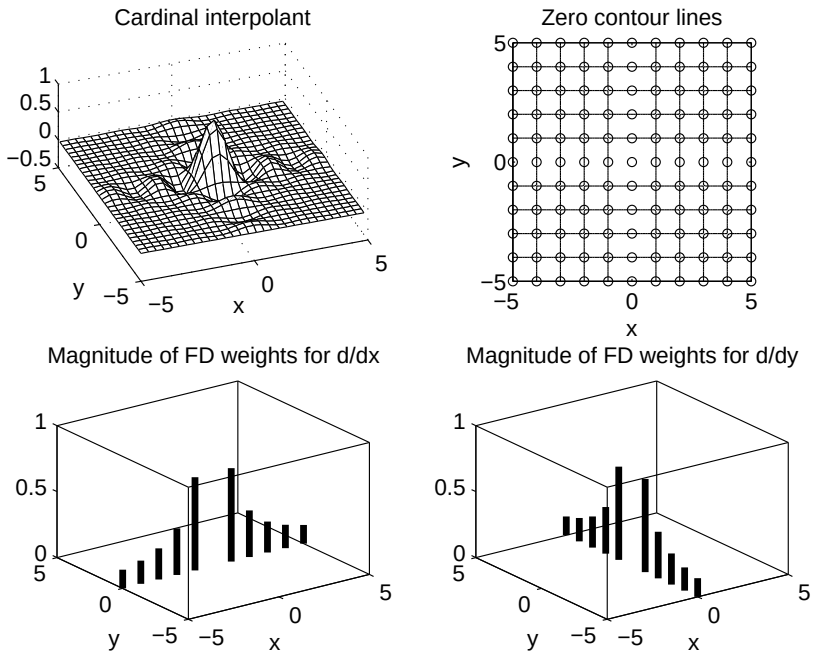

FIG. 10. Key properties of the RBF cardinal interpolant and the generated FD approximations in the case of a Cartesian lattice and $\varepsilon \to 0$.

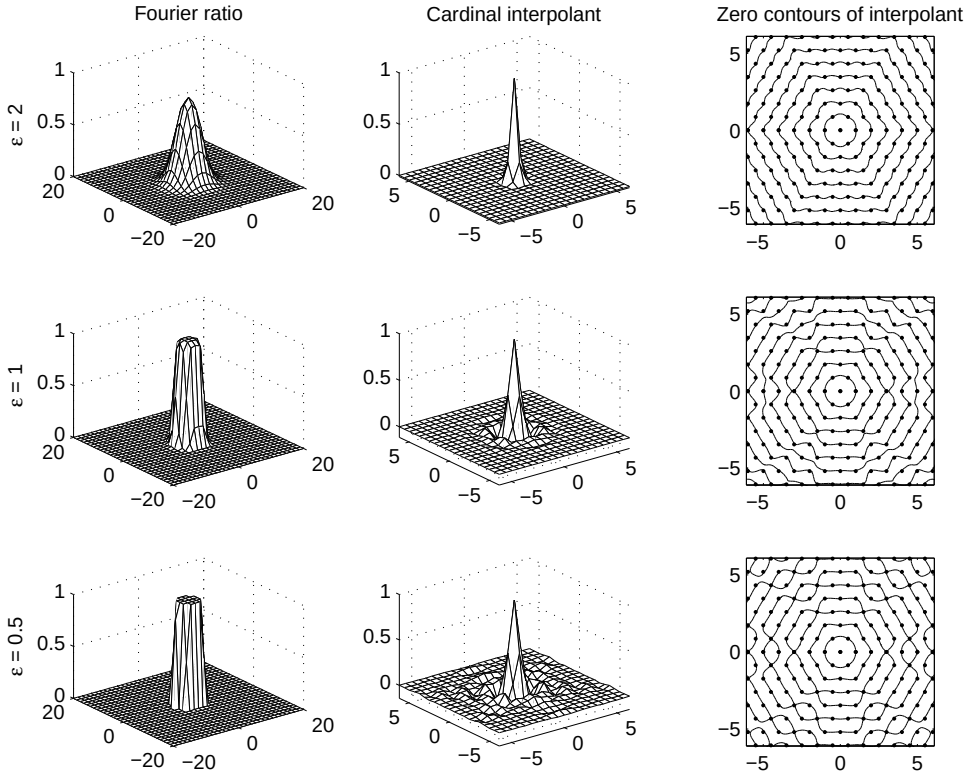

FIG. 11. Fourier ratio $\widehat{\phi}(\xi,\eta)/\Xi_{Hex}$, Cardinal interpolant (on an infinite hexagonal lattice), and its zero contour lines (with the nodes marked by dots) displayed for three cases of GA RBF ($\varepsilon = 2, 1, 0.5$ respectively).

5.2 *Hexagonal lattices*

Hexagonal lattices have sometimes been used in connection with low order FD methods, although never with PS methods. In the context of RBFs, Iske (Iske (2000), Iske (2004)) described this node distribution as 'optimal'. Nevertheless, it has received relatively little subsequent attention.

5.2.1 *Cardinal functions and resulting FD weights for $\varepsilon > 0$* The counterparts to (5.1) and (5.2) on an infinite hexagonal grid with nodes located at $(x,y) = (k_1 + \frac{1}{2}k_2, \frac{\sqrt{3}}{2}k_2)$, k_1, k_2 integers, is

$$c(x,y) = \frac{\sqrt{3}}{8\pi^2} \int_{-\infty}^{\infty}\int_{-\infty}^{\infty} \frac{\widehat{\phi}(\xi,\eta)\cos x\xi \ \cos y\eta}{\Xi_{Hex}(\xi,\eta)} d\xi d\eta \tag{5.4}$$

where

$$\Xi_{Hex}(\xi,\eta) = \sum_{k=-\infty}^{\infty}\sum_{l=-\infty}^{\infty} \widehat{\phi}(\xi + 4\pi(k+\tfrac{1}{2}l), \eta + \tfrac{2\pi}{\sqrt{3}}l). \tag{5.5}$$

is based on a hexagonal summation pattern in Fourier space. The results in Figure 11 were obtained by direct numerical evaluation of (5.4) and (5.5). The left column of subplots should be compared to

Figure 6 b. The most notable difference is that, if ε is made smaller, the ratio $\widehat{\phi}(\xi,\eta)/\Xi(\xi,\eta)$ this time approaches a hexagonal based (rather than square based) step function. The middle column of subplots shows the corresponding cardinal interpolants. We note that these are very local in character when ε is large. For smaller values of ε, they extend much further out, in particular along the primary lattice directions (as we will see shortly in Figure 13). Since the corresponding FD weights are proportional to the partial derivatives of this cardinal interpolant at the node points, larger ε corresponds to more local stencils. The rightmost column of subplots in Figure 11 should be compared to the counterparts in Figures 7, 8, 9 and 10. As is obviously required, all node points (apart from the one at the origin) have at least one zero contour line going exactly through it. We can note that the zero contour line connectivity pattern changes significantly when ε varies.

5.2.2 *Smooth RBFs in the limit of* $\varepsilon \to 0$ For the same reason that $\widehat{\phi}(\xi,\eta)/\Xi(\xi,\eta)$ approached a constant within a square region (and zero outside it) in the Cartesian case (Figure 3), the corresponding limit in the hexagonal case will feature the constant non-zero value within a hexagonal domain in the ξ,η-plane. The double integral (5.4) can in this limit be evaluated in closed form, giving

$$c(x,y) = -\frac{3}{4\pi^2(x^3-3xy^2)}\,[2x\cos(\frac{4\pi x}{3})- \\ -(x-\sqrt{3}y)\cos(\frac{2\pi}{3}(x-\sqrt{3}y))-(x+\sqrt{3}y)\cos(\frac{2\pi}{3}(x+\sqrt{3}y))] \tag{5.6}$$

Figure 12 shows the counterparts to Figures 10 for the Cartesian lattice case (note that the x,y-lattice in the surface plot of the cardinal function bears no relation to the hexagonal node lattice). Figure 13 shows the cardinal interpolant in much greater detail, clearly revealing its ray-type character.

We have at this point several possible explanations of the fact that RBF approximations frequently (but not always) are observed to be most accurate at some finite value of ε rather than in the $\varepsilon \to 0$ limit:

1. As noted in connection with Figure 11, large ε approximations tend to be more local in nature - intuitively reasonable since a derivative is a local property of a function. The ray structure seen in Figure 13 is not 'physical' but a grid artifact. It emerges only in the last stages of the $\varepsilon \to 0$ process. Earlier, the decay is exponential in all directions rather than (slow) algebraic in certain ones.

2. As seen when comparing Figures 8 and 10, large ε approximations can pick up information that is missed in the $\varepsilon = 0$ (PS) case.

3. In case boundaries are present, $\varepsilon \to 0$ is likely to lead to Runge phenomenon type edge effects, which typically cause an increase in errors (Fornberg & Zuev (2007)).

6. Scattered nodes and periodic domains

There are several reasons to believe that somewhat scattered node layouts for RBFs also can be very effective. Such reasons include

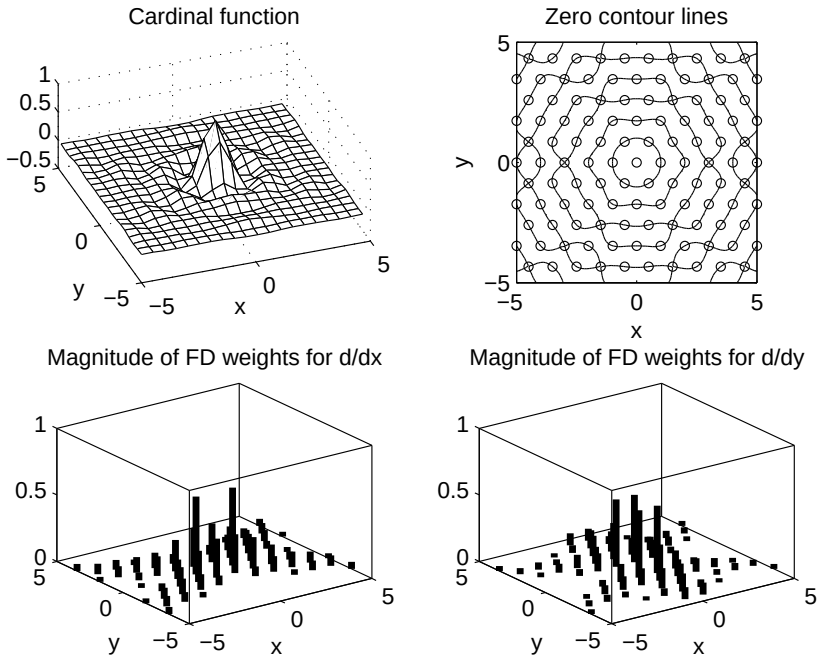

FIG. 12. Key properties of the RBF cardinal interpolant and generated FD approximations in the case of a hexagonal lattice in the $\varepsilon \to 0$ limit.

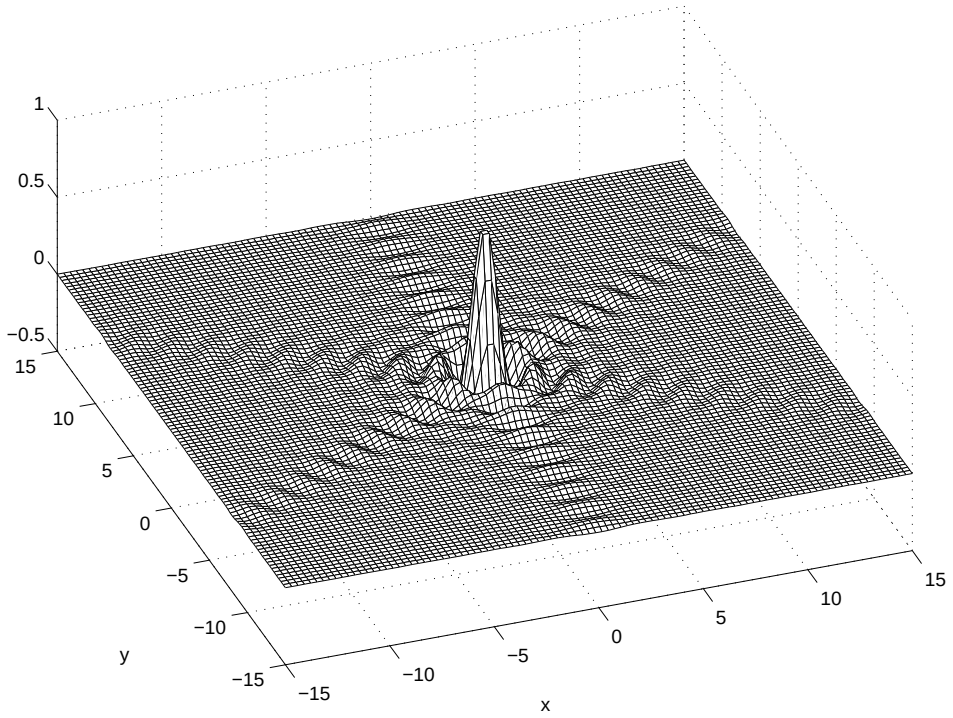

FIG. 13. The cardinal RBF interpolant as $\varepsilon \to 0$ on a unit-spaced hexagonal grid, as described by (5.6). This function is the same as the one shown in the top left subplot of Figure 12, but displayed over a larger domain in order to better illustrate its ray-like character.

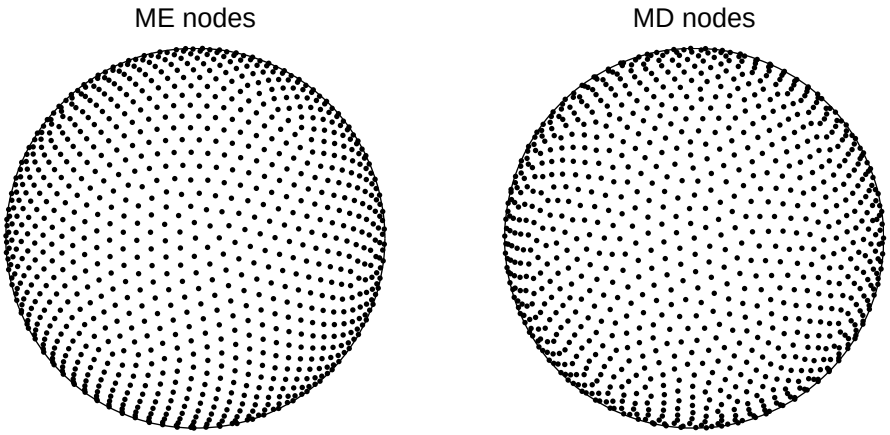

FIG. 14. Comparison between ME and MD node layouts on the sphere (in the case of $n = 1849$ nodes)

1. As discussed in Fornberg et al. (2004), it suffices to place five nodes along a line and the RBF interpolant, as $\varepsilon \to 0$, will diverge to infinity off the line. In 2-D, the same phenomenon arises on rectangular lattices of sizes 5 or larger in either direction (Driscoll & Fornberg (2002)) (GA RBF form an exception (Fornberg et al. (2004), Schaback (2005)); most likely the Bessel class of RBFs discussed in Fornberg et al. (2006) forms the most general class of exceptions). These observations point towards Cartesian lattice type node layouts being prone to singularities that are never encountered with scattered nodes.

2. On the sphere, RBF interpolants typically approach SPH interpolants as $\varepsilon \to 0$ (Fornberg & Piret (2007)), which are singular for a vast number of node layouts (for example, if the data is given on a longitude-latitude grid). Minimal energy (ME) distributed nodes (as obtained by freely-moving equal point charges repelling each other) form patterns with a hexagonal lattice resemblance (Figure 14 a), and SPH interpolation then becomes very close to singular - although not exactly so. Womersley & Sloan (2001) found that SPH interpolation accuracy can be improved by many orders of magnitude by changing from ME (minimal energy) to so-called MD (maximal determinant) node sets (Figure 14 b), which have a more irregular appearance than the ME node set.

Since both analytical and numerical results are difficult to obtain in cases of scattered node on infinite domains, we will instead focus the following discussion on numerical tests on 2-D doubly periodic domains (which also are free from boundary effects).

6.1 *RBFs on periodic domains*

There are two main approaches for implementing RBFs on periodic domains, as illustrated below for 1-D and 2-D domains.

6.1.1 *1-D periodic domain*

Say that the domain is $[-\pi, \pi]$:

1. Modify $\phi(r)$ to make it periodic. Instead of $\phi(r)$, we use as basis functions the sums of periodic repetitions
$$\psi_1(r) = \sum_{k=-\infty}^{\infty} \phi(r+2\pi k). \tag{6.1}$$
Collocation using $\psi_1(r)$ instead of $\phi(r)$ will produce a 2π-periodic interpolant. As an often preferable alternative to summing (6.1) directly, it can be evaluated by means of its (generalized) Fourier transform and Poisson's summation formula (Fornberg & Flyer (2005)).

2. Instead of placing the nodes (denoting them for now θ_k, $k = 1,\ldots,n$) along a straight line, we can place them around a unit circle $z_k = e^{i\,\theta_k}$, and implement RBFs in 2-D. The distance between the nodes θ_i and θ_j then becomes $2\sin\frac{\theta_i-\theta_j}{2}$, so this procedure can be thought of as staying in 1-D and using as radial function
$$\psi_2(r) = \phi(2\sin\frac{r}{2}).$$

The two approaches above, both accommodating for periodicity, are not equivalent. The second approach has the advantage that standard theory for non-singularity immediately applies. No singularities have been observed with the first approach, but confirming theory does not yet appear to be available.

6.1.2 *2-D doubly periodic domain* With basis functions centered at $x = x_c$, $y = y_c$, on $[-\pi,\pi]\times[-\pi,\pi]$, the first approach generalizes to
$$\psi_1(x-x_c,y-y_c) = \sum_{k=-\infty}^{\infty}\sum_{l=-\infty}^{\infty} \phi(\sqrt{(x-x_c+2\pi k)^2+(y-y_c+2\pi l)^2}). \tag{6.2}$$

In the second case, one possibility would be to embed a torus in 3-D space. A simpler, and maybe more natural option is to use
$$\psi_2(x-x_c,y-y_c) = \phi(2\sqrt{\sin^2(\tfrac{x-x_c}{2})+\sin^2(\tfrac{y-y_c}{2})}). \tag{6.3}$$

While (6.3) can be evaluated directly for all choices of RBFs and values of ε, (6.2) is mainly convenient in the GA case for large values of ε. Immediate use of (6.2) gives then rapid convergence of the double sum. For small values of ε, Poisson's summation formula (referred to above in Section 6.1.1) leads again to a rapidly convergent representation

$$\begin{aligned}
\psi_1(x-x_c,y-y_c) &= \sum_{k=-\infty}^{\infty}\sum_{l=-\infty}^{\infty} e^{\,-\varepsilon^2[(x-x_c+2\pi k)^2+(y-y_c+2\pi l)^2]} \\
&= \left(\sum_{k=-\infty}^{\infty} e^{\,-\varepsilon^2(x-x_c+2\pi k)^2}\right)\left(\sum_{l=-\infty}^{\infty} e^{\,-\varepsilon^2(y-y_c+2\pi l)^2}\right) \\
&= \frac{1}{4\pi\varepsilon^2}\sum_{k=-\infty}^{\infty}\sum_{l=-\infty}^{\infty}\left(e^{\,-\frac{1}{4\varepsilon^2}(k^2+l^2)}\,e^{\,-i(k\,x_c+l\,y_c)}\right)\,e^{i\,(kx+ly)}
\end{aligned}$$

where the last line follows from the identity
$$\sum_{k=-\infty}^{\infty} e^{-\varepsilon^2(r+2\pi k)^2} = \frac{1}{2\varepsilon\sqrt{\pi}}\sum_{k=-\infty}^{\infty} e^{-\left(\frac{k}{2\varepsilon}\right)^2}\,e^{ikr}.$$

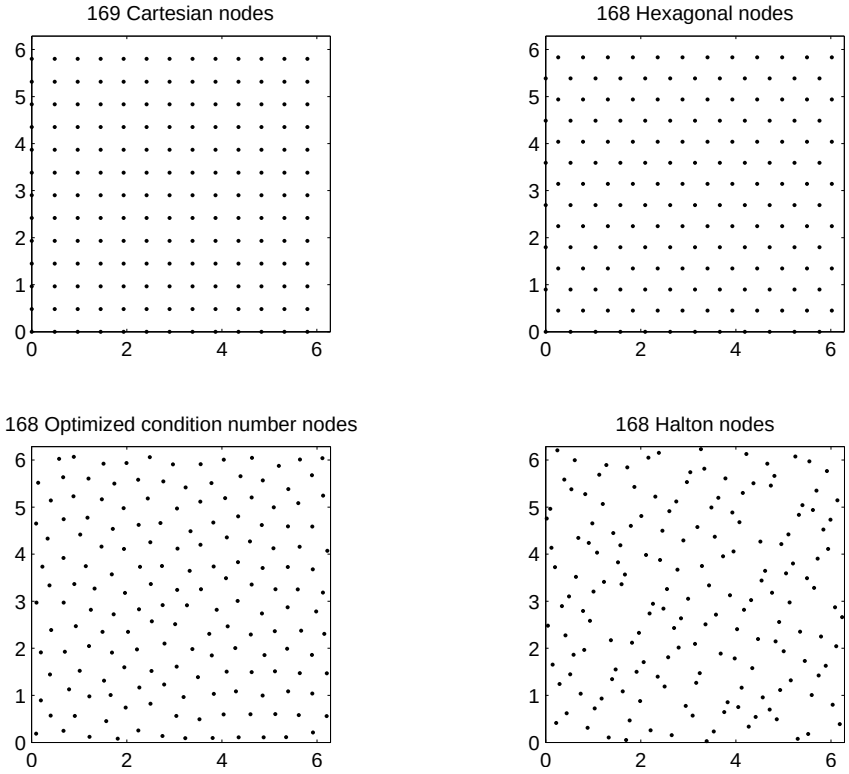

FIG. 15. The four different periodic node distributions over $[0,2\pi]\times[0,2\pi]$ that we use for numerical comparisons.

6.2 *Different 2-D periodic node distributions*

Figure 15 shows four different periodic node distributions over $[0,2\pi]\times[0,2\pi]$. The first one is purely Cartesian, with $13^2 = 169$ nodes. The second is a very close approximation to a hexagonal layout, with 168 nodes. The nearest neighbor distances vary with about 4% (a perfect hexagonal layout is impossible on a periodic square). For these two distributions, the condition numbers of the RBF A-matrix in the case of GA with $\varepsilon^2 = 0.2$ are $1.28\cdot 10^{14}$ and $1.30\cdot 10^{11}$ respectively. With Matlab's genetic algorithm tool, we can perturb the hexagonal pattern in order to minimize this condition number further, reaching $3.81\cdot 10^{10}$ with the node distribution in the bottom left subplot. A fourth option that has been commonly used both for Monte Carlo simulations and for RBFs are 'Halton points', as explained for example in Appendix A of Fasshauer (2007). The condition number for GA $\varepsilon^2 = 0.2$ in this case is $6.13\cdot 10^{13}$. These four node distributions are used in the following numerical tests.

6.3 *Numerical tests on a 2-D periodic domain*

For the tests described below, we implemented GA for (6.2) and both GA and MQ for (6.3). No significant difference was found between the results (just as only minor differences were found in Flyer & Wright (2007) and Fornberg & Piret (2008) between different smooth RBF types). As a result, it is

sufficient to present the case of GA using (6.3).

6.3.1 *Fourier mode treatment by the different node sets* The cardinal interpolant formulas (5.1) and (5.4) were illustrated in Fourier space in Figure 6 b and in the left column of subplots of Figure 11 for Cartesian and hexagonal grids, respectively. These were all infinite lattice results, and it is not clear how to obtain counterparts to these in cases of scattered nodes. We therefore turn to a 2-D periodic geometry, where we can proceed numerically as illustrated in Figure 16. Using each of the four node sets shown in Figure 15, we interpolate a wide range of 2-D Fourier modes (GA, $\varepsilon = 2$) and then, over a much denser grid, calculate the correlation coefficient between the Fourier modes and their RBF interpolants. If a mode is correctly represented, this coefficient will evaluate to one, whereas it otherwise will become close to zero. The middle row of subplots in Figure 16 shows these results. The leftmost two subplots are very reminiscent of the infinite lattice results, but we are now also obtaining the similar functions associated with scattered nodes. Since there are no 'special' directions in the scattered node cases, contour lines (with the 0.9 level illustrated in the bottom row of subplots) become then nearly circular. We showed earlier in Section 3.2 that if a function is band limited within a circular domain in Fourier space, the weights for approximating derivatives are global. The last two subplots in the bottom row of Figure 16 show that scattered nodes lead to this situation.

Although it is unclear how much conclusions can be drawn from Figure 16, it might still be interesting to make a few heuristic observations. In the last two cases ('optimized' and 'Halton'), the irregularities seem to have an adverse effect on the accuracy (as seen most clearly at the zero base level in the middle row of subplots). Comparing the 'Cartesian' and 'hexagonal' cases, we focus instead on the bottom row of subplots, and observe near-square and near-hexagonal domains in Fourier space, which can be shown to be of the same area when $\varepsilon \to 0$. In 3-D, we would similarly get a cube and a multifaceted sphere approximation of matching volumes. In D dimensions, the main diagonal in a hypercube is $\sqrt{D}$ times the side length, suggesting that the anisotropy in the Cartesian case worsens quite rapidly for increasing D.

6.3.2 *Accuracy comparisons in case of a 2-D periodic test function: Fixed number of nodes* Figure 17 illustrates how the max norm error varies with ε when we interpolate the test function

$$f(x,y) = \frac{1}{\left(1 + \left(\sin\frac{\pi - x}{2}\right)^6 + \left(\sin\frac{\pi - y}{2}\right)^6\right)^4} \tag{6.4}$$

with the four 2-D periodic node point sets. Matlab's regular 'double precision' worked well down to $\varepsilon = 0.3$ and, for lower values of ε, we instead used its VPA (variable precision arithmetic) in order to ensure results free from ill conditioning effects. The results are entirely consistent with the different aspects of analysis presented above (although we here consider interpolation rather than derivative approximation). In particular, the hexagonal lattice gives the best accuracy, with a non-zero optimal ε-value. Here, the Halton node set comes out as the worst of the four sets - most likely since the node locations are so irregular that they at some places form very tight groups and at other places leave quite large areas without any nodes at all. The Cartesian node set does not work very well either with the main reason most certainly being its weaker approximation qualities in certain spatial directions as noted in Section 5.1. The 'optimized' node set was optimized only in terms of the GA condition number at one fixed ε value. Although it did not in this particular test perform any better than the hexagonal node set, it

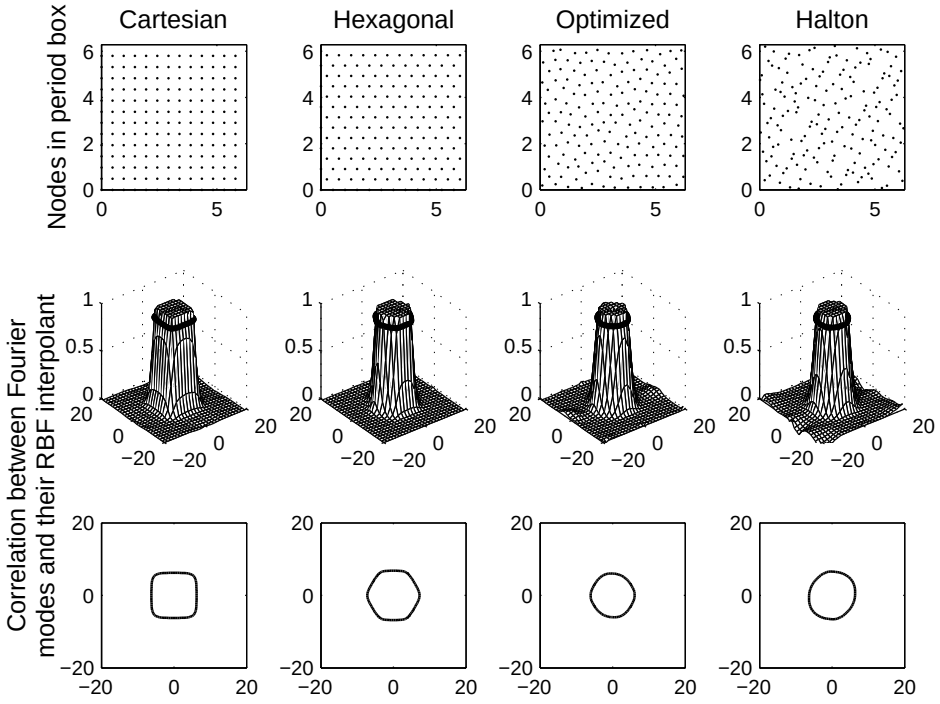

FIG. 16. Illustration of the Fourier modes that are present when using different node layouts in a 2-D periodic domain. Top row: The same node distributions as illustrated in Figure 15. Middle row: Correlation coefficients between 2-D Fourier modes and their RBF interpolants, Bottom row: Regions (in 2-D Fourier space) inside which the correlation coefficients exceed 0.9.

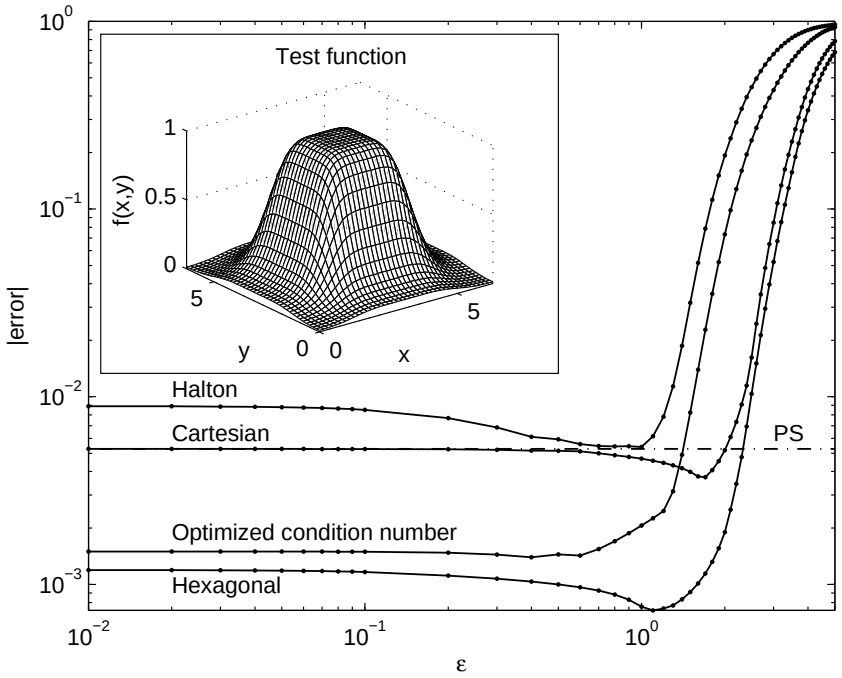

FIG. 17. Errors (in max norm over the domain), as function of ε, when the 2-D periodic test function (6.4) is approximated by RBFs using different node distributions. The horizontal dashed line shows the Fourier-PS error level (same as for Cartesian RBFs in the $\varepsilon \to 0$ limit).

nevertheless confirmed that scattered node sets can be clearly better than Cartesian ones. The Cartesian RBF case, in its $\varepsilon \to 0$ limit, reproduces the standard Fourier-PS method - cf. the dashed line in Figure 17. The hexagonal RBF case with an optimal ε (just above one) gives nearly an order of magnitude lower error.

6.3.3 *Interpolation errors when increasing the number of nodes* As noted earlier, RBF approximations are typically of spectral accuracy when there is no adverse Runge phenomenon is present. Our second numerical test case is designed to test this spectral convergence. We consider the same test function (6.4), but vary the number of nodes N, choosing in each case a numerically determined 'optimal' ε. In place of the 'optimized condition number' node set, we introduce instead fully random sets, as illustrated in Figure 18. Just using independent uniformly distributed random numbers as node coordinates causes severe local clusterings, and rather large areas can lack nodes entirely. Although it is not likely to be a good strategy, it will nevertheless provide interesting comparisons. The result of this test is seen in Figure 19 (computed with RBF-Direct, using GA RBFs in standard 64-bit double precision floating point). For all the four types of node distributions, the errors follow largely linear trends in this log-linear plot, confirming spectral accuracy (the horizontal axis is chosen as $\sqrt{N}$ since this quantity in

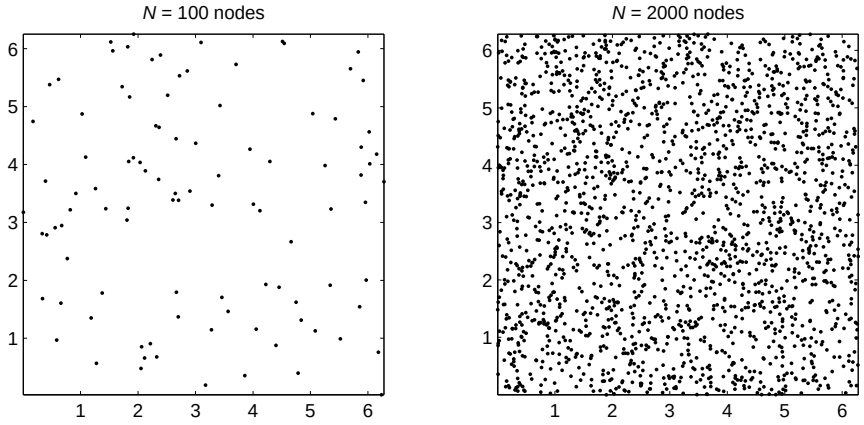

FIG. 18. Typical examples of the highly irregular character of node layouts when the the x and y positions of the nodes are independent random numbers

2-D becomes inversely proportional to the typical node distances). The fully random node distribution is seen to be the worst. The severe node irregularities have damaged the accuracy, but maybe less so than might have been expected. The Cartesian case features a strange oscillatory pattern and a clearly disappointing performance, especially given how commonly it is used in the literature (always in PS and often in RBF contexts). The Halton distributions perform relatively well. However, the hexagonal layout is clearly the best of the four choices.

The differences between the four cases may seem relatively small, but they are nevertheless noteworthy in bringing out seldomly recognized problems with Cartesian node layouts. For interpolation of an unknown periodic function in 1-D (i.e. with nothing known that could be utilized for local node refinement), an equispaced grid is likely to be optimal. The results in Figure 19 illustrate that the issue in 2-D is a lot more complicated, and that it would be shortsighted to just assume that a Cartesian 2-D grid is the preferable generalization from 1-D. Although 1-D analysis often can give valuable insights, great care has to be exercised when such results are transferred to two or more dimensions. For the heuristic reasons indicated in Section 6.3.1, going to 3-D will likely further increase the differences between the two primary layouts this study has focused on; Cartesian vs. hexagonal.

6.3.4 *Derivative errors when increasing the number of nodes: Comparison with the Fourier-PS method*
For this test, we choose the test function shown in the top left subplot of Figure 20

$$f(x,y) = \frac{(2-\cos x)(2-\cos y)}{3+\cos 2x + 0.2\sin(x+3y) + 0.5\cos y} \tag{6.5}$$

somewhat reminiscent of Matlab's 'peaks'-function, but 2π-periodic in both x and y. The methods we include now are the two best ones from the previous test (RBFs on Halton and hexagonal node sets) and compare against standard Fourier-PS on a 2-D Cartesian grid. The computations were done with both GA and MQ RBFs, with virtually identical results (the MQ results are shown in the figure). Again, the

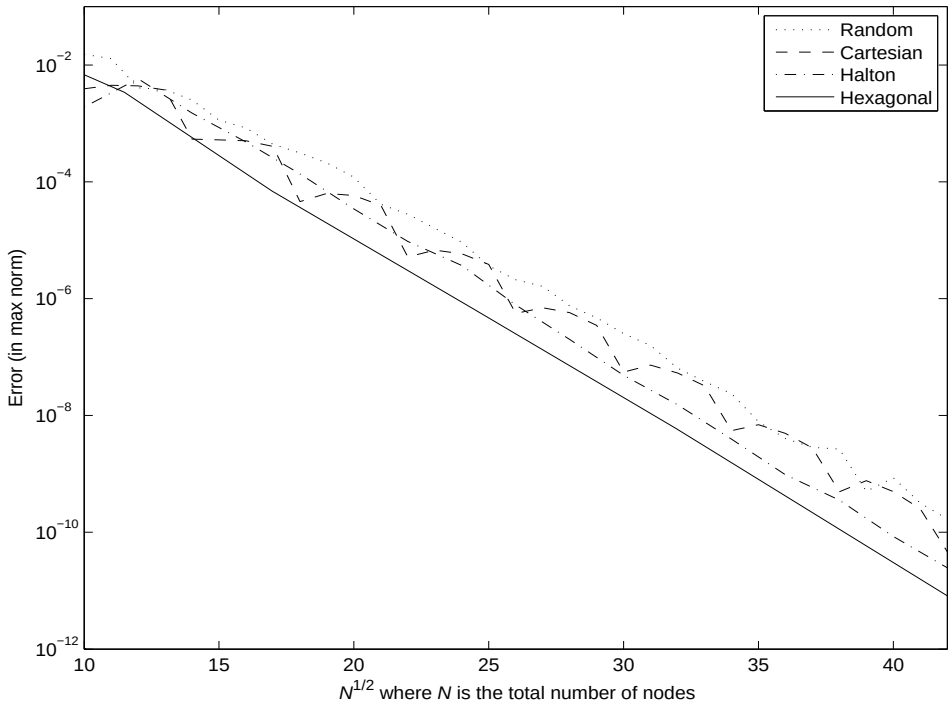

FIG. 19. Maximum norm errors in the same test case as shown in Figure 17 for four different types of node distributions using GA RBFs.

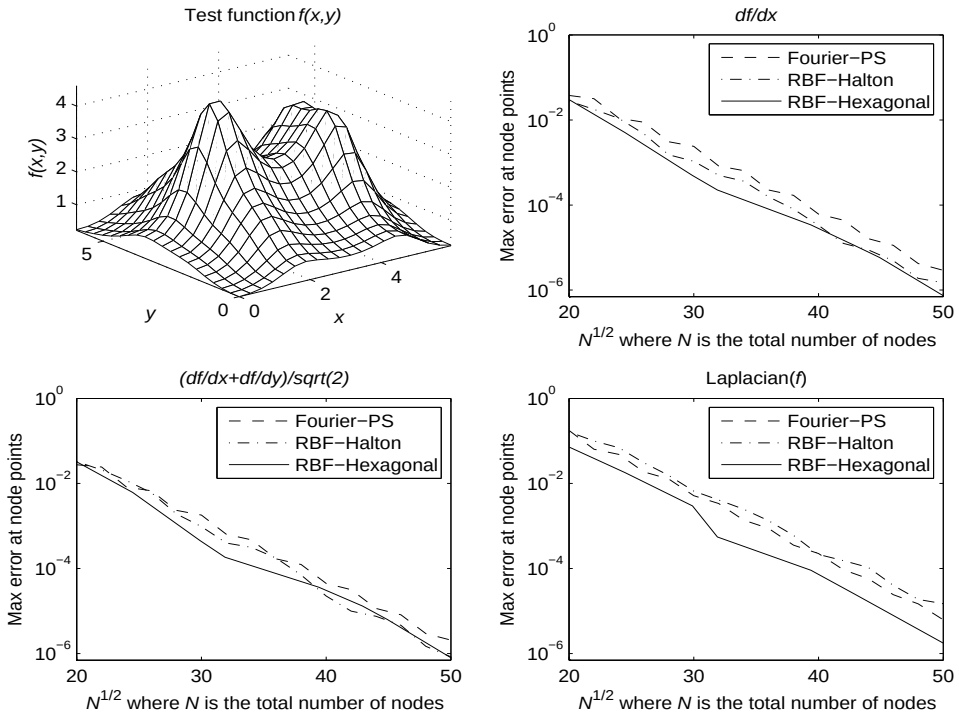

FIG. 20. Top left subplot: The test function 6.5. Remaining three subplots: The largest error at a node point (compared against the analytical values) for the quantities $\frac{\partial f}{\partial x}$, $\frac{1}{\sqrt{2}}\left(\frac{\partial f}{\partial x}+\frac{\partial f}{\partial y}\right)$, $\frac{\partial^2 f}{\partial x^2}+\frac{\partial^2 f}{\partial y^2}$, respectively when using MQ RBFs.

differences between the compared methods are not vast, but they are still clear and consistent enough to make the point that, even in a 2-D periodic geometry, Fourier-PS is not the optimal method in terms of the accuracy it provides for a fixed number of node points.

We did not in these comparisons include any node sets generated by 'greedy' algorithms. Such iterative algorithms successively adds or subtracts nodes according to some strategy that appears plausible at each instant (for example, by placing a new node wherever the error is the largest). Brief discussions can be found in Fasshauer (2007) and Wendland (2005). The resulting node sets often become quite irregular - visually on a similar level as Halton node sets. While this level of irregularities may well be acceptable, keeping the computational cost relatively low may be a challenge.

7. Conclusions

As we have stressed repeatedly in this study, the overwhelming strength of RBF methods relates to their spectral accuracy also in the presence of irregular boundaries in two or more dimensions, their ability to incorporate very flexible versions of local node refinement, etc. We have here tried to shed some light - largely for theoretical insight only - on two cases in which RBFs typically would *not* be used for practical computing: infinite lattices and periodic domains. In the former case, we have provided Fourier analysis suggesting that hexagonal grids may be advantageous over Cartesian ones - confirming

earlier made observations based on different arguments. The latter case (2-D periodic domains) is the most ideal setting possible for Fourier-PS methods. Our tests show that even then, RBF approximations are capable of providing somewhat higher accuracy for the same number of nodes. We also note that even high levels of irregularities (as featured for example by Halton-type node sets) cause only very minor accuracy degradations.

8. Acknowledgements

The first author (BF) gratefully recalls numerous discussions over the years with Professor Ron Mitchell, on topics related to derivative approximations in general as well as on other subjects. We also acknowledge discussions with Tyger (Susan) Hovde, Dr. Cécile Piret and Prof. Berne Maxum.

The work of Bengt Fornberg was supported by the NSF Grants DMS-0611681 and ATM-0620068. The work of Natasha Flyer was supported by NSF Grant ATM-0620100. The National Center for Atmospheric Research (NCAR) is sponsored by the National Science Foundation. Jennifer M. Russell, Major, United States Air Force, was supported by the Department of Defense. The views expressed in this article are those of the authors and do not reflect the official policy or position of the United States Air Force, Department of Defense, or U.S. Government.

REFERENCES

BAXTER, B.J.C. (1992) On the asymptotic cardinal function of the multiquadric $\varphi(r) = (r^2 + c^2)^{1/2}$ as $c \to \infty$, *Comp. Math. Appl.* **24** , 1–6.

BUHMANN, M. D. (2003) *Radial Basis Functions*, Cambridge, U.K. ; New York : Cambridge University Press.

BUHMANN, M. D. & POWELL, M.J.D. (1990) Radial basis function interpolation on an infinite regular grid, In: J. C. MASON AND M. G. COX, eds. *Algorithms for Approximation II,* London ; New York : Chapman and Hall, 146–169.

DRISCOLL, T.A. & FORNBERG, B. (2002) Interpolation in the limit of increasingly flat radial basis functions, *Comp. Math. Appl.,* **43**, 413–422.

FAIRWEATHER, G. & MITCHELL, A.R. (1967) A new computational procedure for ADI methods, *SIAM J. Num. Anal.*, **4** , 163–170.

FASSHAUER, G.E. (2007) *Meshfree Approximation Methods with Matlab*, World Scientific Publishing, Singapore.

FLYER, N. (2006) Exact polynomial reproduction for oscillatory radial basis functions on infinite lattices, *Comp. Math. Appl.* **51**, 1199–1208.

FLYER, N. & LEHTO, E. (2008) A radial basis function implementation of local node refinement: Two vortex test cases on a sphere, submitted to *Roy. Met. Soc. Quar. Jour.*.

FLYER, N. & WRIGHT, G. (2007) Transport schemes on a sphere using radial basis functions, *J. Comp. Phys.*, **226**, 1059–1084.

FLYER, N. & WRIGHT, G. (2008), A radial basis function shallow water model, submitted *J. Comp. Phys.*.

FORNBERG, B. (1996) *A Practical Guide to Pseudospectral Methods*, Cambridge; New York : Cambridge University Press.

FORNBERG, B., DRISCOLL, T.A., WRIGHT, G. AND CHARLES, R. (2002) Observations on the behavior of radial basis functions near boundaries, *Comp. Math. Appl.*, **43**, 473–490.

FORNBERG, B. AND FLYER, N. (2005) Accuracy of radial basis function interpolation and derivative approximation on 1-D infinite grids, *Adv. Comp. Math.*, **23** , 5–20.

FORNBERG, B. AND FLYER, N. The Gibbs phenomenon for radial basis functions. In *The Gibbs Phenomenon in Various Representations and Applications*, ed. A. Jerri, Sampling Publishing, Potsdam, NY.

FORNBERG, B., FLYER, N., HOVDE, S. AND PIRET, C. (2008) Locality properties of radial basis function expansion coefficients for equispaced interpolation, *IMA J. Num. Anal.*, **28**, 121–142.

FORNBERG, B., LARSSON, E. AND WRIGHT, G. (2006) A new class of oscillatory radial basis functions, *Comp. Math. Appl.*, 1209–1222.

FORNBERG, B. AND PIRET, C. (2007) A stable algorithm for radial basis functions on a sphere, *SIAM J. Sci. Comp.*, **30**, 60–80.

FORNBERG, B. AND PIRET, C. (2008) On choosing a radial basis function and a shape parameter when solving a convective PDE on a sphere, *J. Comp. Phys.*, **227**, 2758–2780.

FORNBERG, B., WRIGHT, G., & LARSSON, E. (2004) Some observations regarding interpolants in the limit of flat radial basis functions, *Comp. Math. Appl.*, **47**, 37–55.

FORNBERG, B. & WRIGHT, G. (2004) Stable computation of multiquadric interpolants for all values of the shape parameter, *Comp. Math. Appl.*, **48**, 853-867.

FORNBERG, B. & ZUEV, J. (2007) The Runge phenomenon and spatially variable shape parameters in RBF interpolation, *Comp. Math. Appl.*, **54**, 379–398.

GOURLAY, A.R. & MITCHELL, A.R. (1969) The equivalence of certain alternating direction and locally one-dimensional difference methods, *SIAM J. Num. Anal.*, **6** , 37–46.

GOURLAY, A.R. AND MITCHELL, A.R. (1969) A classification of split difference methods for hyperbolic equations in several space dimensions, *SIAM J. Num. Anal.*, **6**, 62–71.

ISKE, A. (2000) Optimal distribution of centers for radial basis function methods. Report, Technische Universitat, Munchen.

ISKE, A. (2004) *Multiresolution Methods in Scattered Data Modeling*, Springer Verlag, Berlin.

LARSSON, E. AND FORNBERG, B. (2003) A numerical study of radial basis function based solution methods for elliptic PDEs, *Comp. Math. Appl.*, **46**, 891–902.

MITCHELL, A.R. AND FAIRWEATHER, G. (1964) Improved forms of the ADI methods of Douglas, Peaceman and Rachford for solving parabolic and elliptic equations, *Numer. Math.*, **6**, 285–292.

POWELL, M.J.D. (1992) The theory of radial basis function approximation in 1990, in *Advances in Numerical Analysis, Vol. II: Wavelets, Subdivision Algorithms and Radial Functions*, W. Light, ed., Oxford University Press, Oxford, UK, 105–210.

SCHABACK, R. (2005) Multivariate interpolation by polynomials and radial basis functions, *Constr. Approx.*, **21**, 293–317.

WENDLAND, H. (2005) *Scattered Data Approximation*, Cambridge University Press, Cambridge.

WOMERSLEY, R.S. & SLOAN, I. (2001) How good can polynomial interpolation on the sphere be? *Adv. Comp. Math.*, **14**, 195–226.